

Nanostructured Black Silicon as a Stable and Surface-Sensitive Platform for Time-Resolved In Situ Electrochemical Infrared Absorption Spectroscopy

Felix Rauh,* Johannes Dittloff,* Moritz Thun, Martin Stutzmann, and Ian D. Sharp*

Cite This: *ACS Appl. Mater. Interfaces* 2024, 16, 6653–6664

Read Online

ACCESS |

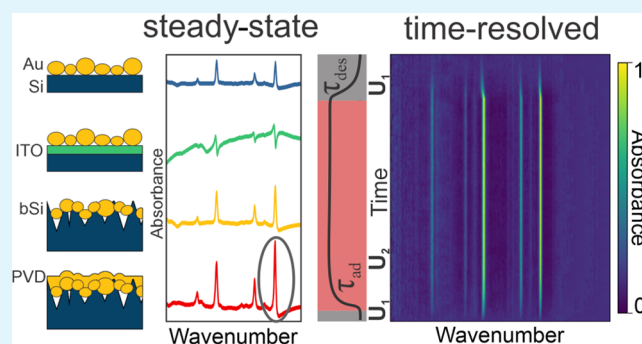
Metrics & More

Article Recommendations

Supporting Information

ABSTRACT: Attenuated total reflection surface-enhanced infrared absorption spectroscopy (ATR-SEIRAS) is a powerful method for probing interfacial chemical processes. However, SEIRAS-active nanostructured metallic thin films for the in situ analysis of electrochemical phenomena are often unstable under biased aqueous conditions. In this work, we present a surface-enhancing structure based on etched black Si internal reflection elements with Au-coatings for in situ electrochemical ATR-SEIRAS. Using electrochemical potential-dependent adsorption and desorption of 4-methoxypyridine on Au, we demonstrate that black Si-based substrates offer advantages over commonly used structures, such as electroless-deposited Au on Si and electrodeposited Au on ITO-coated Si, due to the combination of high stability, sensitivity, and conductivity. These characteristics are especially valuable for time-resolved measurements where stable substrates are required over extended times. Furthermore, the low sheet resistance of Au layers on black Si reduces the RC time constant of the electrochemical cell, enabling a significantly higher time resolution compared to that of traditional substrates. Thus, we employ black Si-based substrates in conjunction with rapid- and step-scan Fourier transform infrared (FTIR) spectroscopy to investigate the adsorption and desorption kinetics of 4-methoxypyridine during in situ electrochemical potential steps. Adsorption is shown to be diffusion-limited, which allows for the determination of the mean molecular area in a fully established monolayer. Moreover, no significant changes in the peak ratios of vibrational modes with different molecular orientations relative to the molecular axis are observed, suggesting a single adsorption mode and no alteration of the average molecular orientation during the adsorption process. Overall, this study highlights the enhanced performance of black Si-based substrates for both steady-state and time-resolved in situ electrochemical ATR-SEIRAS, providing a powerful platform for kinetic and mechanistic investigations of electrochemical interfaces.

KEYWORDS: ATR, SEIRAS, black Si, Au nanoparticles, time-resolved IR spectroscopy, in situ IR spectroscopy



INTRODUCTION

The importance of understanding electrochemical interface processes is continuously growing, driven in part by the increasing interest in renewable energy and energy storage technologies, such as (solar) water splitting, battery technologies, and electrocatalytic synthesis of sustainable fuels.¹ To advance these applications, a key need is to gain mechanistic insights into interfacial processes via real-time in situ spectroscopy, which enables direct observation of reaction intermediates or degradation processes under operating conditions. In this regard, infrared absorption spectroscopy is a particularly powerful technique due to its sensitivity to molecular vibrations, which enables the identification of specific chemical bonds at the interface. Therefore, this technique is especially relevant for the observation of catalytic processes, such as CO₂ reduction catalysis,^{2–6} or for photoelectrochemical water splitting.^{7,8} In particular, time-resolved studies provide the ability to observe reaction

intermediates, quantify kinetics, and understand dynamic changes to reaction microenvironments, all of which are critically important for understanding the behavior of electrochemical interfaces.⁹ However, a major limitation of Fourier transform infrared (FTIR) spectroscopy is its lack of surface sensitivity, which can be partially overcome by using the attenuated total reflection (ATR) geometry to achieve a micrometer-scale sampling depth. Even higher surface sensitivity can be realized by the use of metallic films for

Received: November 17, 2023

Revised: December 20, 2023

Accepted: December 22, 2023

Published: January 24, 2024



surface-enhanced infrared absorption spectroscopy (SEIRAS), which extends sensitivity down to the nanometer-scale.

A common geometry for in situ electrochemical ATR-FTIR experiments is the Kretschmann configuration in which the internal reflection element (IRE) also serves as the working electrode. Since the surface of the IRE comprises the substrate under investigation, it must simultaneously fulfill the requirements imposed by the FTIR measurement and the catalytic system. Due to the involved complexity, most investigations have so far been limited to processes occurring on thin (<100 nm) metallic films deposited on Si or Ge IREs, with the most common systems being based on Au thin films deposited onto Si IREs using a variety of different techniques.^{10–13} Such systems allow for acceptable transmission in the fingerprint region of the IR spectrum and exhibit superior chemical stability due to the use of a noble metal on a relatively inert substrate. In addition, nanostructuring the Au thin film can yield dramatic improvements to surface sensitivity due to local field enhancement caused by plasmonic interactions and the lightning rod effect.¹⁴ The resulting ATR-SEIRAS configuration allows for analysis of the immediate vicinity (<10 nm) of the substrate surface, enabling the measurement of (sub-) monolayer coverages of organic compounds and intermediate states, as well as reaction microenvironments.

Such nanostructured Au films have been shown to enable valuable insights into a variety of catalytic processes. The nanostructuring necessary for the surface enhancement is usually achieved via electroless deposition,^{11,15–17} electro-deposition,¹³ colloidal self-assembly,¹⁸ or physical vapor deposition,^{10,19,20} sometimes accompanied by electrochemical surface roughening.^{12,21} Other metals, including a variety of Pt group metals,^{22,23} Ag,²⁴ and Cu,²⁵ have also been successfully implemented for in situ FTIR studies. While these layers generally lead to sufficient surface enhancement, they often suffer from poor adhesion to the underlying IRE substrate. This leads to a high probability of spontaneous delamination during the measurement, which limits the accessible electrochemical potential range during in situ measurements, precludes long-term studies, and adversely affects reproducibility. Furthermore, films rarely survive dismounting from the electrochemical cell, which makes it impossible to characterize electrode surfaces following in situ experiments and prevents repetitive measurements of individual surfaces. A solution to this issue is the use of an adhesion layer, such as Ti, between Si and Au. While such structures have been reported,²¹ it has also been shown that the presence of the adhesion layer suppresses the surface enhancement effect.¹³

The demand for a widely applicable, robust, and reproducible IRE substrate design that simultaneously offers high surface sensitivity and electrochemical stability has motivated the development of alternative structures, most notably those that use transparent conductive oxides (TCOs) as adhesion promoters. In addition, electrical conductivities of such films enable the integration of electrodeposited Au layers.^{13,26} While such strategies enhance the mechanical adhesion of subsequently deposited Au structures, they also introduce a new material with limited chemical stability. In particular, achieving efficient surface enhancements requires a nanostructured morphology, the porosity of which can easily leave the TCO exposed and vulnerable to degradation if the conditions extend beyond the stability window of the oxide.²⁷ Considering the chemical susceptibilities of the most commonly used TCOs, which include indium tin oxide

(ITO), indium zinc oxide (IZO), and fluorine-doped tin oxide (FTO),^{27–29} this can severely limit the accessible range of surface potentials and pH values during in situ electrochemical FTIR experiments. To overcome these stability limitations, an alternative method based on boron-doped diamond (BDD) thin films to replace the TCO layer was recently reported and shows exceptional stability over a broad range of electrochemical potentials.³⁰ While such BDD layers offer great promise for in situ studies, they also require specialized chemical vapor deposition reactors for fabricating the coatings and are characterized by spectral absorption in the 1100–1300 cm⁻¹ range, which could interfere with some measurements. Furthermore, the comparatively high resistivities of the diamond layers and TCOs lead to long RC time constants that limit the temporal resolution of such electrodes for time-resolved in situ electrochemical measurements. While this can be partially addressed by microstructuring to reduce the associated capacitance,³¹ this comes at the cost of reduced solid/liquid contact area and IR light coupling efficiency.

In the present work, we demonstrate an alternative strategy to achieve highly robust and surface-sensitive IREs for advanced in situ electrochemical FTIR experiments. These substrates are generated via nanostructuring of the IRE using a wet-chemical method that was originally developed as a surface treatment to reduce reflective losses of solar cells.^{32–34} The resulting nanomorphology, known as black Si, offers an increased surface area and high roughness, which greatly enhances Au adhesion compared to planar Si surfaces, allows for measurements over a wide potential range for at least 10 h of operation, and significantly increases the solid/liquid contact area. Using reversible adsorption of a 4-methoxypyridine (MOP) monolayer¹⁶ as a benchmark measurement, we show that the additional nanostructuring leads to significantly improved stability without sacrificing surface sensitivity compared to traditional approaches. In addition, the presented structure offers higher electrical conductivity compared with TCO-based substrates. This greatly reduces the series resistance of the electrochemical system and therefore provides dramatically faster electrochemical response times, thereby enabling time-resolved measurements down to the single-digit millisecond range when combined with advanced FTIR measurement techniques. Importantly, the low sheet resistance of the reported IRE ensures that the resistance of the electrolyte rather than that of the working electrode limits this response time, opening opportunities for characterizing even faster dynamics by using suitably conductive electrolytes or improved electrochemical cell designs. While time-dependent FTIR studies have been used extensively for observing slower time scales in the range of seconds, studies at such fast time scales are much more scarce^{31,35–37} and typically comprise poorly adhesive planar metallic films. Here, we use the electrochemically robust and surface-sensitive black Si-based IRE substrates as a basis for a time-resolved study of the aforementioned MOP model system, investigating the dependence of adsorption and desorption time constants and molecular orientations on the MOP concentration in the electrolyte. Thus, the presented nanostructured black Si IRE substrates are versatile platforms for both steady-state and time-resolved in situ electrochemical FTIR. Overall, this work paves the way for intricate mechanistic studies with high stability, reproducibility, and submonolayer sensitivity.

■ EXPERIMENTAL SECTION

IRE Surface Preparation. The commercial IREs used in this study are based on Si wafers (Specialized 1, Iruibis) that feature periodic microstructures on their backsides to facilitate in- and out-coupling of IR light and minimize reflective losses. This geometry provides significant advantages in terms of reduced cost, improved handling, and decreased absorption losses compared with traditional ATR crystals. All substrates were cleaned by ultrasonication in acetone (ULSI grade, Microchemicals) and subsequently in isopropyl alcohol (ULSI grade, Microchemicals) for 10 min each. After sonication, each substrate was thoroughly rinsed with isopropyl alcohol and dried under a stream of nitrogen. The remaining contaminants were removed by oxygen plasma treatment for 10 min at 200 W. These cleaning processes were performed immediately before further processing steps to minimize the time for the reabsorption of contaminants.

Black Si (bSi) Etch. Black Si surfaces were produced by a wet-chemical etching process adapted from Branz et al.³⁴ To begin with, the native oxide covering the Si surface was removed by immersion in a 5% hydrofluoric acid (HF, 50% Technic) solution for 2 min. This treatment leads to metastable hydrogen termination of the Si surface. The surface structuring was performed immediately after HF treatment by consecutively placing a series of solutions on the surface. In particular, a 100 μ L droplet of 0.4 mM aurochloric acid (HAuCl_4 , 49% Au basis, Sigma-Aldrich), followed by a 100 μ L droplet of 1.7% HF and 20% hydrogen peroxide (H_2O_2 , 31%, BASF) were placed on the surface for 5 min to form the black Si. Care was taken to ensure that the backside of the substrate was kept pristine and did not come into contact with the etching solution. An in-depth description of this preparation process, as well as the involved reaction mechanisms, was previously reported by Branz et al.³⁴ After the black Si etch, the backside can be more robustly protected by covering it with a photoresist (S1818, Microposit). We note that this protection layer could not be applied earlier in the processing sequence due to incompatibility with the solvent and plasma cleaning steps. Furthermore, protection directly after cleaning could have led to increased surface contamination and was therefore omitted in favor of the aforementioned droplet technique. Finally, the surface structure was refined by etching in a 0.4% potassium hydroxide (KOH, 85% KOH basis, Sigma-Aldrich) solution at slightly elevated temperatures of 30 $^\circ\text{C}$ for 10 s.³⁸

Electroless (EL) Deposition of Au. The electroless deposition process described in the following is based on the previous work of Miyake et al.¹¹ and is briefly summarized here. Similar to the black Si etching procedure, electroless deposition begins by immersion of the sample in a 5% HF solution for 2 min. The substrates were then immersed in a 1:1:1 mixture of three solutions containing 2% HF, 0.3 M sodium sulfite (Na_2SO_3 , 97% Merck) with 0.1 M sodium thiosulfate ($\text{Na}_2\text{S}_2\text{O}_3$, 99.5% Sigma-Aldrich) and 0.1 M ammonium chloride (NH_4Cl , 99.5% Sigma-Aldrich), and 30 mM sodium tetrachloroaurate (NaAuCl_4 , 99% Sigma-Aldrich) mixed in the mentioned order. This mixture was preheated to 50 $^\circ\text{C}$, after which the substrates were immersed in it for 35 s. After deposition, the substrates were first dried under a stream of nitrogen, then rinsed in copious amounts of ultrapure deionized water, and dried again. The protective photoresist-coating on the backside of the sample was subsequently removed by immersion in acetone and isopropyl alcohol, followed by final drying with nitrogen.

Electroless deposition was performed on two different types of substrates: (i) on polished Si surfaces to replicate the most prevalent substrate structure from the literature,¹¹ and (ii) on substrates that were pretreated with the black Si etching procedure. These latter substrates were either used directly after electroless deposition or further processed by thermal evaporation of an additional 30 nm-thick Au layer. This additional evaporated Au layer was intended to increase the in-plane electrical conductivity of the film and to cover any exposed Si.

Electrodeposition (ED) of Au. The electrodeposition described in the following is adapted from Andvaag et al.¹³ A design allowing for

homogeneous and repeatable electrodeposition requires a conductive layer on the Si substrate, which by itself is not sufficiently electrically conductive for the investigated time-resolved FTIR measurements due to its low doping concentration. Thus, a 50 nm ITO layer was sputtered onto the polished Si substrate prior to electrodeposition to serve as a conducting adhesion layer. This layer was annealed at 400 $^\circ\text{C}$ in air for 1 h to improve conductivity and IR transparency.³⁹ Afterward, the substrate was mounted inside a three-electrode electrochemical cell with the ITO-coated Si serving as the working electrode. An Au wire and a low leakage Ag/AgCl (Driref-2SH, World Precision Instruments) electrode were used as the counter and reference electrodes, respectively. Potentials were applied to the IRE working electrode by using an Interface 1010E potentiostat (Gamry Instruments). The geometric area exposed to the electrolyte was 0.125 cm^2 . Electrodeposition of Au nanoparticles was initialized by a set of three cyclic voltammetry scans (CVs) from -1 to 1 $V_{\text{Ag/AgCl}}$ at a sweep rate of 20 mV s^{-1} . The electrolyte contained 0.1 M sodium fluoride (NaF, 99% Sigma-Aldrich), 250 μM sodium tetrachloroaurate (NaAuCl_4 , 99%), and 100 μM 4-methoxypyridine (97%, Sigma-Aldrich). Further scans were performed at the same sweep rate, but the potential window was reduced to a maximum potential of 0.05 $V_{\text{Ag/AgCl}}$ in the positive direction. The electrochemical cell was mounted in the spectrometer during electrodeposition, which allowed for in situ monitoring of the emerging MOP signal as the enhancement by the electrodeposited Au layer increased. For such in situ probing of the surface enhancement, the substrate was held at 0.3 $V_{\text{Ag/AgCl}}$ for 60 s after every three sets of CVs to record a reference FTIR spectrum. The potential was then stepped to -0.9 $V_{\text{Ag/AgCl}}$ and held for 60 s to record the sample spectrum. Proceeding with too many electrodeposition cycles led to a decrease in the signal, presumably due to deposition of thick Au layers. Therefore, the process was stopped as soon as the saturation of the signal enhancement was observed. This was generally the case after approximately 40 CV cycles. It is important to note that in contrast to the electroless deposition procedure, only a portion of the ITO surface was exposed to the electrodeposition solution. In particular, no Au was deposited outside the O-ring that defined the solid/liquid contact. While this area was identical to the IR-probed solid/liquid interface during MOP ad-/desorption measurements, electrical contact to the sample was made near the edge of the sample. Therefore, a portion of the electrical current path was through bare ITO not coated with Au, leading to a comparatively large series resistance.

Steady-State and Time-Dependent In Situ FTIR. FTIR measurements were carried out with a Vertex 70v vacuum spectrometer (Bruker Optics GmbH & Co. KG) using a global light source and a liquid nitrogen-cooled photovoltaic mercury cadmium telluride detector. The substrate was mounted at the bottom of a home-built gastight electrochemical cell (Figure S1) that was inserted into the sample chamber before evacuation to a base pressure of below 1 mbar. The chamber was evacuated for at least 30 min before any measurements were initiated to ensure sufficiently stable conditions, in particular for step-scan measurements. The external angle of incidence was chosen to be 55 $^\circ$ following prior investigations by Morhart et al. regarding the signal intensity for such an IRE design.⁴⁰ The setup was aligned carefully to ensure maximum throughput with minimal introduction of stray light from the surrounding support structure. For steady-state spectra, both reference and sample measurements were collected by averaging 128 scans with a spectral resolution of 4 cm^{-1} .

Steady-state measurements of the adsorption and desorption of MOP were first performed to determine the sensitivities of different IRE substrates. An aqueous solution containing 100 mM LiClO_4 (98%, Sigma-Aldrich) and 100 mM MOP served as the electrolyte. Before it was transferred to the electrochemical cell, the electrolyte was bubbled with N_2 in order to displace dissolved CO_2 and O_2 . A final cleaning and conditioning step was performed by running 10 CV scans in the range of -1.1 to 0.5 $V_{\text{Ag/AgCl}}$ using the identical electrochemical setup described above. Afterward, IR spectra were recorded at -0.9 $V_{\text{Ag/AgCl}}$ and subsequently at 0.3 $V_{\text{Ag/AgCl}}$. Over the

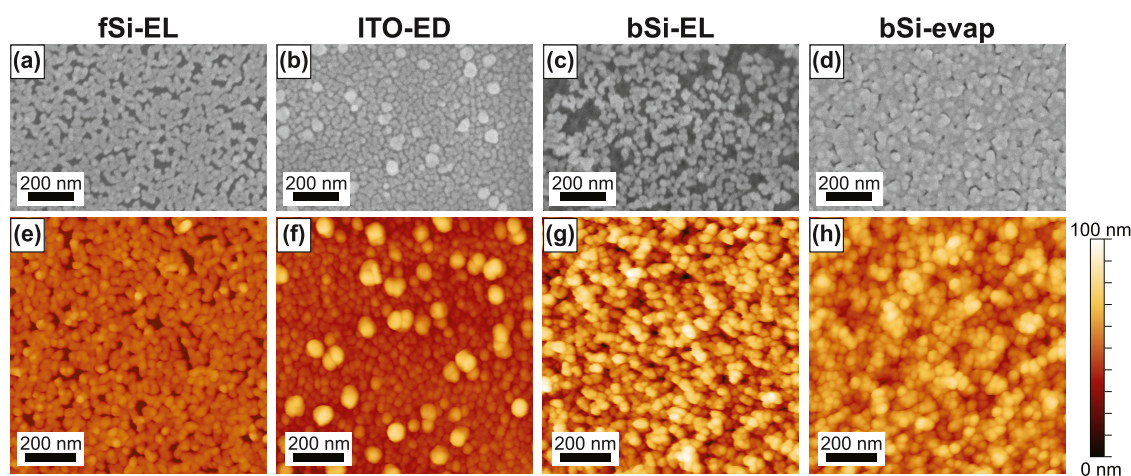


Figure 1. Comparison of the surface morphologies of all investigated IRE substrates, measured via SEM (a–d) and AFM (e–h). (a, e) Electroless Au deposited on flat, polished Si (fSi-EL). (b, f) Electrodeposited Au on ITO on polished Si (ITO-ED). (c, g) Electroless Au deposited on black Si (bSi-EL). (d, h) Electroless Au deposited on black Si with an additional layer of evaporated Au (bSi-evap).

range of MOP concentrations presented here, these potentials are expected to be below and above the de-/adsorption potentials of MOP on Au, respectively. All subsequently presented data sets follow the convention of using the measurement at desorption potentials as the reference spectrum, which results in a positive absorbance signal for adsorbed molecules.

Based on a prior study, it is assumed that the adsorption process is self-limiting to a single monolayer.²⁶ However, we note that due to the concentration-dependent MOP adsorption isotherm, the 100 mM experiment is near the limit for enabling complete desorption under an applied potential of $-0.9 V_{\text{Ag}/\text{AgCl}}$. To determine whether incomplete MOP desorption has a significant influence on our results, we compared the absolute change of the transient signal upon the potential step for high and low MOP concentrations. For the 100 mM sample, a slight reduction of the signal amplitude by up to 15% was observed, but lies close to the $\sim 10\%$ measurement uncertainty. While we can thus conclude that any impact of incomplete monolayer desorption is small over the investigated MOP concentration range, such effects would likely impact measurements at higher concentrations (>100 mM) for the potential steps investigated here.

Time-dependent in situ FTIR analysis was performed by using the same measurement geometry during potential step electrochemical control. The measurements were carried out by using either the step- or rapid-scan FTIR method (Bruker). For the step-scan, the data recording process is spread over multiple repetitions of the same experiment by acquiring the temporal evolution of the detector signal for a sequence of fixed interferometer positions, thereby allowing the time-resolved interferogram to be constructed. The repetitive nature of this method requires high reproducibility of the experiment since any systematic changes or degradation phenomena can have a severe impact on the final data set. The step-scan measurements in this work were performed by repetitively switching the applied electrochemical potential from -0.9 to $0.3 V_{\text{Ag}/\text{AgCl}}$ and back. This was achieved by making use of an analogue potentiostat (POS2, Bank Electronic) in combination with an arbitrary waveform generator (33250A, Agilent) controlling the timing and communication. The positive potential was held for 164 ms, and the negative potential was held for 41 ms. Step-scan measurements were carried out with a resolution of $50 \mu\text{s}$ over a recording time of 205 ms. The transients recorded at each interferometer position were averaged over five repetitions each. Reference spectra were extracted by averaging 10 spectra recorded immediately prior to the MOP adsorption potential step.

Experiments on longer time scales were performed in a more classical fashion utilizing a rapid-scan during electrochemical chronoamperometry measurements. Here, spectra were consecutively acquired at a high rate by using increased mirror speeds, yielding a time resolution of 60 ms. Time constants were extracted from the data

sets with Bruker's OPUS software. The most prominent MOP peaks at 1615 , 1509 , and 1308 cm^{-1} were analyzed. The background around each peak was fitted with a linear function prior to integration to determine the peak area. Gaussian fits of the background-normalized peaks yielded the positions of each vibrational mode. Time constants were approximated by the half-times of the resulting transients.

Surface Morphology Analysis. The surface morphologies of all IRE substrates were studied using an atomic force microscope (AFM) (Multimode 8, Bruker) in ScanAsyst mode (AFM tips: ScanAsyst Air, 0.4 N m^{-1} spring constant, 1 nm tip radius, Bruker) by scanning surface areas of $1 \times 1 \mu\text{m}^2$. In addition, scanning electron microscopy (SEM) (NVision 40, Zeiss) images were taken at varying magnifications with secondary electrons detected by an in-lens detector.

RESULTS AND DISCUSSION

A total of four different IRE substrates possessing different surface structures and coatings were prepared and are investigated in this work. The substrates were specifically chosen to allow comparison of known and established SEIRAS structures with the newly developed, black Si-based surfaces. The structures chosen as representative benchmarks include the electroless (EL) deposition of Au on a flat, polished Si IRE (fSi-EL) and one based on the electrodeposition (ED) of Au on annealed ITO that was also deposited onto a flat Si IRE (ITO-ED). Two geometries utilizing the novel black Si-structured IREs, one of which includes electroless-deposited gold (bSi-EL) and the other an additional layer of evaporated gold (bSi-evap), are presented and compared. SEM images of the as-prepared black Si surfaces, both before and after KOH treatment, are shown in Figure S2 and exhibit the expected nanostructured morphology.

Surface Morphologies of IRE Substrates. As a starting point for understanding the functional characteristics of the developed IRE substrates, each of their surface morphologies were investigated. The corresponding scanning electron micrographs are shown in Figure 1a–d. All surface treatments led to the generation of Au nanostructures but with somewhat different morphologies. The Au layers created by electroless Au deposition on both polished Si and black Si (Figure 1a,c) share similar particle diameters of $(28 \pm 5) \text{ nm}$, as estimated from analysis of 40 randomly chosen particles for each substrate. Despite the similar particle size, the surface coverage is different for the polished Si substrate compared to the black

Si substrate. The uncovered surface amounts to $\sim 10\%$ of the total area for the layer deposited on polished Si (fSi-EL) and 40% of the total area for the case of black Si (bSi-EL). This is likely a consequence of packing of the Au particles on different substrates. For the fSi-EL substrate, the nanoparticles are more tightly packed within the plane of the surface, whereas for the bSi-EL substrate, the particles tend to agglomerate. For the case of the electrodeposited Au layer on ITO (ITO-ED), the average particle size of (25 ± 4) nm is similar to that of the electroless-deposited structures (Figure 1b). However, a low density of larger particles with a diameter of (57 ± 8) nm is also observed. The resulting electrodeposited Au layer is not completely continuous, and image analysis reveals that $\sim 20\%$ of the underlying ITO surface remains exposed. The morphology of the nanoparticles appears to be more discontinuous, with single particles or clusters of a few particles forming a less interconnected network compared to the electroless-deposited particles. This becomes even more apparent with increased contrast, as shown in Figure S3. The black Si substrates that have been covered in a 30 nm-thick layer of evaporated Au (bSi-evap) after electroless deposition are shown in Figure 1d. As expected, the amount of exposed Si surface is significantly reduced to $\sim 2.5\%$. The continuous nature of the film implies significantly enhanced interconnectivity of individual Au nanostructures. Nevertheless, morphological traces of buried nanoparticles can be recognized underneath the continuous layer.

Complementing SEM, AFM allows the extraction of quantitative information regarding the roughness and surface area of each substrate. AFM micrographs of all four IRE substrates are depicted in Figure 1e–h. The fSi-EL substrate has a root-mean-square (RMS) roughness of 6.2 nm, which is a significant increase from polished Si before electroless Au deposition, which has an RMS roughness of 0.2 nm. As observed in the SEM micrographs, these particles are laterally packed in the plane of the surface and possess an average height of (25 ± 3) nm. This thickness is approximately the same as the in-plane particle size determined from SEM, revealing that the particles are close to spherical in shape. AFM micrographs of the ITO-ED substrate show the two different characteristic particle sizes that were observed with SEM and reveal an RMS surface roughness of 9.3 nm. The more discontinuous arrangement of particles on the surface observed in SEM cannot be resolved using AFM due to the small interparticle spacing, which is obscured by the AFM tip radius. Likewise, the significantly higher surface roughness and sharper features on both black Si substrates make a distinct analysis of the morphology via AFM challenging. The bSi-EL substrate exhibits the highest surface roughness of 13.3 nm, which is reduced to 9.1 nm for the bSi-evap substrate after thermal evaporation. By comparison, AFM measurements indicate a rms surface roughness of 13.5 nm for the bare black Si substrate, though this value is subject to uncertainty due to convolution with the tip dimensions. However, SEM image (Figure S2) analysis of 40 randomly chosen triangular black Si cones enables reliable quantification of the base width and height of these features, which can be estimated to be (44 ± 12) and (36 ± 9) nm, respectively. Finally, it should be noted that we attempted to generate analogous evaporated Au layers on polished Si for a direct comparison of their SEIRAS properties to those of black Si-based structures. However, evaporated Au on polished Si exhibited extremely poor

adhesion and was completely removed upon immersion in water. Therefore, such samples were not further investigated.

Steady-State FTIR Measurements. The SEIRAS performance of the four different IRE substrates during in situ electrochemical FTIR was compared by using adsorbed monolayers of MOP molecules as a model system. This system is suitable for the determination of surface enhancement of a given substrate due to its self-limiting, potential-dependent ad- and desorption through coordination of the free electron pair of nitrogen to a gold surface.¹⁶ The molecular structure of MOP and a reference measurement of bulk randomly oriented MOP molecules, in which all vibrational bands of the MOP molecule are visible, are provided in Figure 2a for comparison. Steady-state IR absorbance spectra

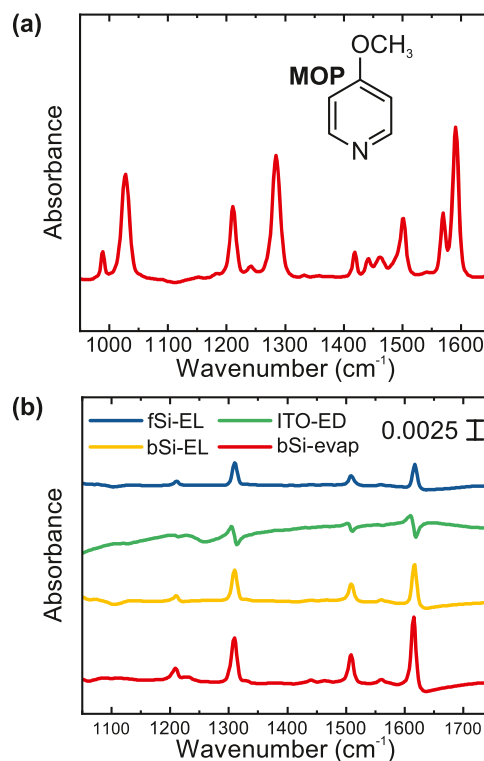


Figure 2. (a) Reference IR absorbance spectrum of bulk MOP on an uncoated Si IRE chip and depiction of the molecular structure of MOP. (b) Steady-state IR absorbance spectra of an MOP monolayer adsorbed on different SEIRAS-active IRE substrates developed here. Variations in peak shapes and signal enhancements are observed as a consequence of different surface morphologies and layer structures, as described in the text.

obtained from all four types of substrates are shown in Figure 2b. Six distinct signals in the range between 1000 and 1700 cm^{-1} are visible for all cases and are consistent with those previously observed from a MOP monolayer adsorbed at a polycrystalline Au/electrolyte interface.^{13,16} The observed vibrational modes correspond to in-plane (A') vibrations of the MOP molecule, with those at 1615, 1562, 1509, and 1211 cm^{-1} attributable to ν_{8a} , ν_{8b} , ν_{19a} , and ν_{9a} ring vibrations, respectively.²⁶ The 1308 cm^{-1} signal can be assigned to the asymmetric C–O–C stretching vibration of the methyl group and that at 1030 cm^{-1} can be attributed to an in-plane ring breathing vibration ν_{12} of the MOP.²⁶

While a flat-lying orientation and binding via interaction with the π -orbital of the molecule has been reported in a

system of dispersed nanoparticles,⁴¹ MOP was previously found to adopt a vertical orientation when adsorbed on polycrystalline Au surfaces under comparable conditions.¹⁶ In such a configuration, the molecules are coordinated to the surface via a σ -type bond between the Au surface and the nonbinding electron pair of the ring nitrogen.¹⁶ Molecular vibrations can be induced and probed in the ATR-SEIRAS geometry only if the transition dipole moment of the vibration has a component normal to the Au surface. Thus, this condition limits the detectable vibrations from the adsorbed MOP monolayer to a subset of IR-active modes. Based on prior results from Quirk et al.,¹⁶ the transition dipole moment of the three most-intense signals at 1615, 1509, and 1308 cm^{-1} share a small angle ($<25^\circ$) to the principal molecular axis, while the band at 1562 cm^{-1} is significantly off-axis. These theoretical results can explain different amplitudes observed here, with the small amplitude of the out-of-plane methyl bands in the 1450 cm^{-1} region being consistent with the vertical adsorption motif.

A broad negative feature at 1650 cm^{-1} , corresponding to the bending mode of water, is present for all three substrates incorporating electroless Au (fSi-EL, bSi-EL, and bSi-evap) and indicates that the adsorption of the MOP monolayer on the Au surface displaces water molecules previously present near the surface. In contrast, the broad spectral background present for the ITO-ED substrate likely masks this feature. Additionally, the fSi-EL and bSi-EL substrates exhibit a small band at 1100 cm^{-1} , which can be attributed to the Si–O–Si asymmetric stretching vibration. This feature can be assigned to slight changes in the surface oxide thickness or its structure during the course of the measurement. The lack of this signal for both the bSi-evap and ITO-ED samples is consistent with the homogeneous coverage and isolation of the underlying Si IRE from the electrolyte. Thus, the absence of such a Si–O–Si feature indicates improved electrochemical stability for these two types of IRE substrates.

All four substrate types can resolve the adsorbed MOP monolayer, although the amplitude and peak shape differ between different substrate types. While the fSi-EL, bSi-EL, and bSi-evap substrates all exhibit symmetric MOP peaks with generally flat backgrounds, the ITO-based ITO-ED substrate is characterized by a broad spectral background and asymmetric peak shapes. Indeed, anomalous lineshapes, including derivative- or Fano-like spectral features similar to those observed here from the ITO-ED substrate, have commonly been obtained during SEIRAS measurements but have been the subject of debate and variously assigned to different physical origins.^{42,43} For the case of discontinuous Au islands on TCOs, Andvaag et al. used an effective medium approach to show that derivative-like features can arise from interface reflectivity changes upon molecular adsorption that are well-described by the Fresnel equations. However, they found that spectral shapes are strongly dependent on the volume fraction of Au within discontinuous overlayers, with such distortions appearing near the percolation threshold and persisting up to an Au volume fraction of approximately 0.37.⁴² Alternatively, such lineshapes can emerge from the coupling of narrow molecular vibrational modes with broad plasmonic modes, which lead to Fano resonances. For the case of ITO, Agrawal et al. observed such coupling over a range of nanostructure sizes.⁴³ In the present work, unambiguous assignment of the physical process underlying the observed lineshapes from the ITO-ED substrates would require additional experiments, such

as polarization- and angle-dependent ATR-FTIR, as well as ITO thickness and Au coverage-dependent measurements, that are outside the scope of the present work. Nevertheless, we note that the presence of a broad spectral background for the ITO-ED substrate may point to a Fano-type mechanism for the Si/ITO/Au structure investigated here.⁴³

In contrast to the ITO-ED substrate, all other IREs investigated here are characterized by positive molecular absorption features. Considering the arguments above, we note that both the fSi-EL and bSi-evap substrates possess large Au coverages that are well beyond the percolation threshold. In contrast, while the discontinuous nature of the agglomerated Au particles on the bSi-EL substrate could lead to complex reflectivity changes upon molecular adsorption, no such anomalous lineshapes are observed here. Thus, we can consider each of these films to behave in a regular fashion, similar to highly reflective Au films, with minimal spectral distortion. Among the investigated substrates, the bSi-EL and bSi-evap substrates exhibit the highest signal intensities under the specific measurement conditions. A likely origin for these higher signal intensities is that the black Si structure introduces nanocavities for impinging IR light, leading to increased light absorption by the Au nanoparticles and, thus, increased plasmonic enhancements.⁴⁴ Nevertheless, it is important to note that the enhancement is subject to large substrate-to-substrate variations that likely arise from the complex nanostructures of the deposited Au layers. Therefore, a significantly larger data set would be needed to compare the surface enhancement of each morphology with statistical confidence. On the basis of the signal-to-noise ratio, we can conclude that all substrates are capable of sensitively detecting molecular adsorbates well below the monolayer limit. In particular, the present measurements reach sensitivities of below 3% of a monolayer for steady-state observation of the 1615 cm^{-1} peak, which was obtained by averaging over 128 scans. However, we note that this does not represent the fundamental limit and could be further enhanced via the optimization of measurement and averaging conditions. Furthermore, the relative ratios between the signal amplitudes of the three most prominent MOP peaks at 1615, 1509, and 1308 cm^{-1} remain comparable for all substrate structures under investigation. This indicates a similar vertical molecular orientation for the adsorbed MOP monolayers on all of the SEIRAS-active substrates.

In addition to the varying degrees of surface enhancement, we observe significant differences in the stabilities of the samples against degradation under the aqueous electrochemical measurement conditions. While the ITO-ED, bSi-EL, and bSi-evap samples did not exhibit degradation under the tested measurement conditions, the fSi-EL samples showed large sample-to-sample variations, and the Au layer was prone to delamination. We note that quantification of the extent of delamination during measurement was difficult but nearly all fSi-EL samples were at least partially delaminated after removal from the electrochemical cell, making this deposition method less suitable for repeated or extended measurements. This increase in stability enabled by the black Si treatment is additionally highlighted through durability tests performed under a strong cathodic bias of $-1.5 \text{ V}_{\text{Ag}/\text{AgCl}}$ in 100 mM LiClO_4 electrolyte for 15 min. As shown in Figure S4, these harsh electrochemical conditions result in catastrophic damage to both the fSi-EL and ITO-ED samples, both of which exhibit substantial delamination of the surface Au layer. Indeed, for the

case of ITO-ED, optical reflectivity measurements reveal near-complete loss of the TCO layer (Figure S5). In contrast, the Au layer on the bSi-EL sample is preserved, and only minor changes of the surface associated with loading and unloading of the electrode from the cell are observed. Thus, we confirm that the black Si treatment provides enhanced stability over a broad range of electrochemical potentials, even prior to the application of the evaporated Au layer.

Time-Dependent FTIR. Time-resolved in situ FTIR measurements are important for providing additional insights into electrochemical kinetics and reaction pathways, potentially enabling the identification of rate-limiting steps in the catalytic energy conversion process. Therefore, we now move beyond steady-state measurements and investigate the viability of IRE substrates for time-resolved FTIR spectroscopy. We note that a similar analysis has been previously reported by Morhart et al.³¹ but was focused on the rate of MOP diffusion away from the surface after desorption using an ITO-based micro-electrode sample probed with a synchrotron IR source. In contrast, we focus on the newly developed black silicon structure, which allows a comparable analysis with a lab-based FTIR system while extending the analysis to both adsorption and desorption kinetics.

For time-resolved studies, the series resistance associated with the working electrode sheet resistance can negatively impact the RC time constant of the complete electrochemical system, which can limit the observation of fast processes. The sheet resistances of different substrates investigated in this work are provided in Figure S6 and highlight the significantly increased conductivity of the bSi-evap substrate compared to all other substrates. This increased in-plane conductivity is a consequence of the more continuous Au film created through thermal evaporation. In contrast, the nanostructured morphology of the other substrates reduces their in-plane conductivities due to the need for current to transfer across nanoparticle boundaries, thereby negatively impacting their ability to deliver charge carriers to the electrochemical interface at a sufficiently fast rate. In general, the bulk Si of the supporting IRE substrate does not add considerably to electronic conduction because its low doping concentration leads to high specific resistances. While higher doping would lead to lower resistances, this should be avoided, since it would come at the cost of reduced IR transmittance. For the case of the ITO-ED substrate, the ITO layer also provides an in-plane electrical conductivity transport path. However, its specific conductivity depends on the chosen synthesis parameters and is, in general, much smaller than the specific conductivity of Au (by roughly a factor of 100–1000), especially for thin films of thicknesses well below 100 nm.^{39,45,46} This is especially relevant for the case of the ITO-ED substrate since Au deposition is limited to the region of solid/liquid contact and the electrical current path to the external contact is through bare ITO, as described in the Experimental Section.

To assess the impacts of different conductivities of IRE working electrodes on the minimum response time of the electrochemical system, we monitored the change of electrical current during potential step experiments in the 100 mM LiClO₄ electrolyte. This investigation is limited to the two substrate designs deemed most suitable for time-resolved studies. In particular, fSi-EL was excluded due to inferior sample stability, while bSi-EL was excluded due to its significantly lower conductivity and smaller surface enhancement compared to the bSi-evap substrates. The limiting time

resolutions were evaluated on the basis of the electrical current half-times ($\tau_{1/2}$). Importantly, we find that the current half-time of the bSi-evap substrate of 3.6 ms is more than a factor of 2 faster than the time constant of the ITO-based substrate of 7.5 ms, as depicted in Figure 3a. Improved RC time constants

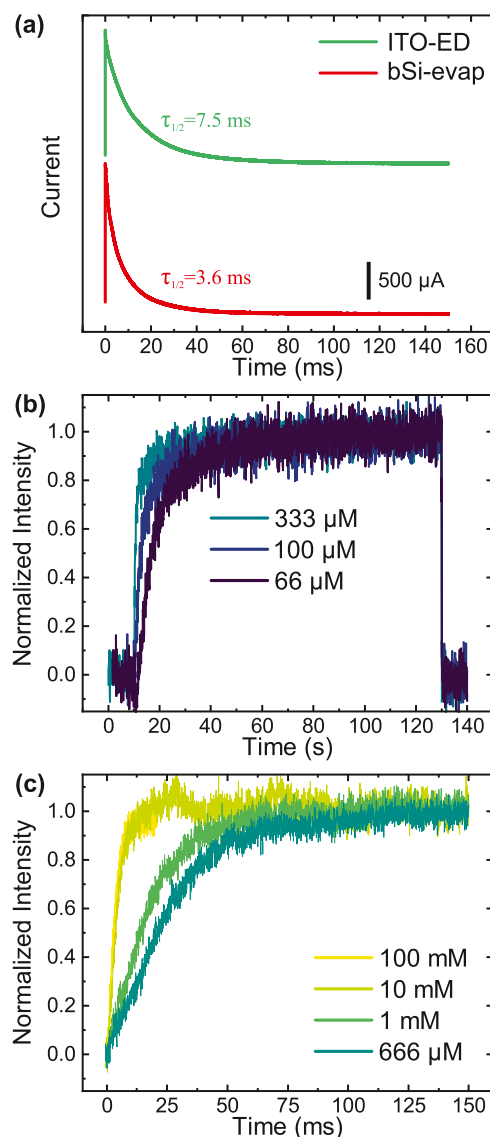


Figure 3. (a) Current transient measurements of a bSi-evap and an ITO-ED substrate upon a potential step from -0.9 to 0.3 V_{Ag/AgCl} in the identical in situ electrochemical measurement setup but in the absence of MOP, indicating a faster RC time constant for the bSi-evap substrate. (b) Increase and decrease of the 1615 cm⁻¹ peak intensity over the course of an ad- and desorption rapid-scan FTIR experiment at lower MOP concentrations. (c) Time-dependent increase of the 1615 cm⁻¹ peak intensity during potential step-induced MOP adsorption for high MOP concentrations recorded with step-scan FTIR.

can therefore be achieved with the newly developed bSi-evap substrate without the need for electrode miniaturization, which would significantly reduce infrared light transmission, alter mass transport during in situ measurements, and require elaborate photolithographic processing. In addition, we emphasize that the RC time constant for measurements using the bSi-evap sample is not limited by the sheet resistance

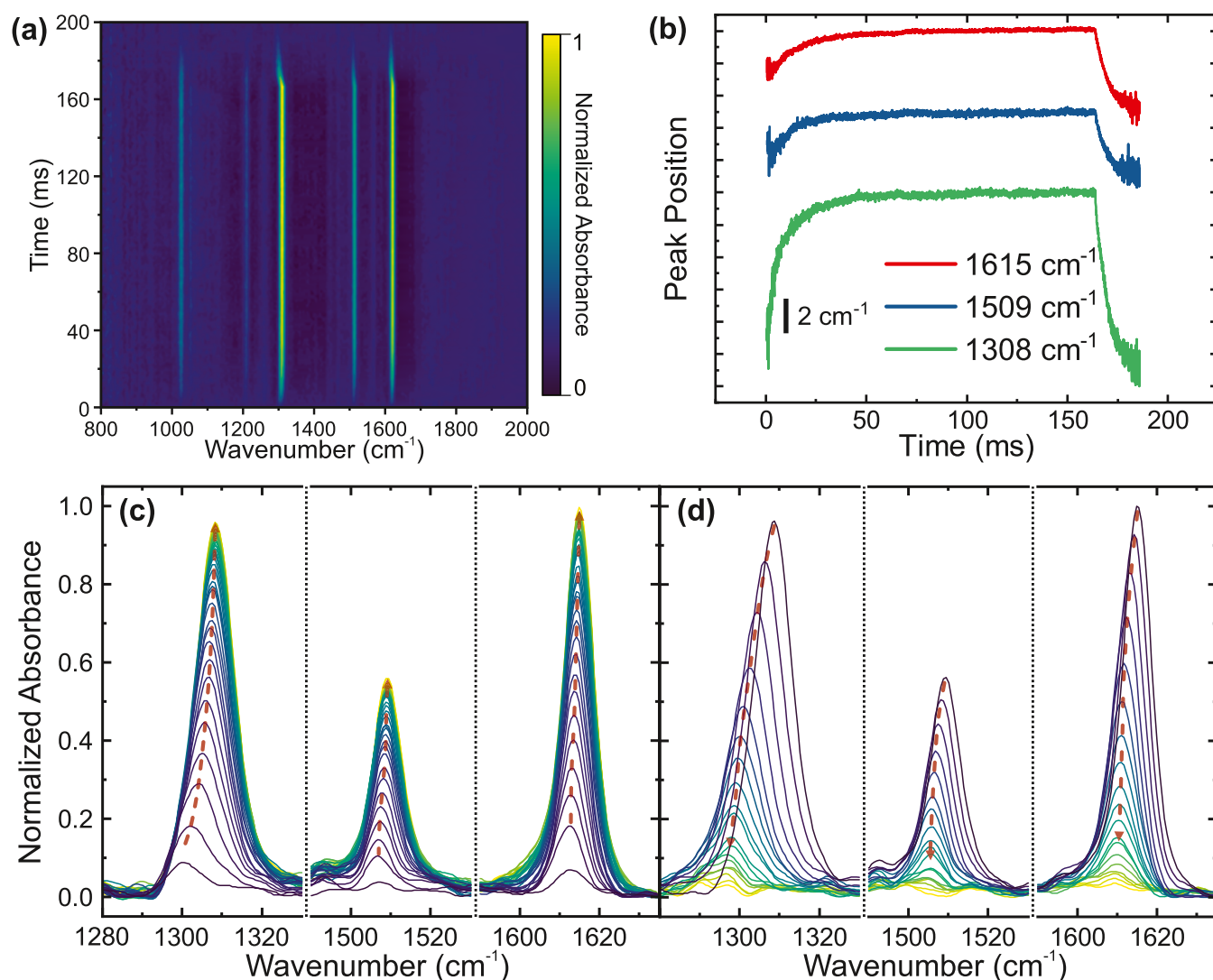


Figure 4. (a) 2D representation of the temporal evolution of IR spectra for a 1 mM concentration of MOP recorded using the step-scan method. (b) Peak position change relative to its equilibrium value for the three main spectral features during adsorption and desorption. (c, d) Selected spectra extracted at 2 ms intervals for the aforementioned transitions depicting the evolution of the spectral shape over time. Arrows indicate the direction of the time evolution.

of the working electrode itself but rather by the resistance of the electrolyte. In particular, the sheet resistance of the bSi-evap sample is a factor of 100 smaller than that of the ITO-ED sample, while both have similar surface roughness values of 9.1 and 9.3 nm, respectively, leading to similar interfacial capacitances. Thus, one would expect that the electrode-limited RC time constant for bSi-evap should be on the order of 100 times faster than that for the ITO-ED electrode. However, only a factor of 2 improvement in the response time is observed. This apparent discrepancy can be resolved by considering the influence of the 100 mM LiClO₄ electrolyte resistivity, combined with the macroscopic geometry of the electrochemical cell. Indeed, reference measurements performed using 1 M LiClO₄ reveal an order of magnitude decrease of the electrical current response time of the electrochemical cell to $\sim 300 \mu\text{s}$. Thus, unlike the case of the ITO-ED sample, the observed half-time for the bSi-evap IRE is not a fundamental limit of the electrode itself, but instead of the electrochemical cell, which can be independently optimized via use of more concentrated electrolytes or cell designs with reduced interelectrode dimensions.

Here, this powerful combination of high spectral sensitivity, temporal responsivity, and chemical stability of the bSi-evap substrate was applied to study the time-dependent adsorption and desorption of MOP monolayers in order to gain insight into the kinetics of this system as a function of the concentration of MOP in the electrolyte. In particular, FTIR spectral dynamics were analyzed in situ during the application of electrochemical potential steps in electrolytes containing bulk MOP concentrations ranging from 66 μM up to 100 mM. The resulting evolution of the most prominent molecular vibrational mode at 1615 cm⁻¹ on the surface of bSi-evap working electrodes was analyzed. The resulting data show a change in adsorption time constants over 3 orders of magnitude as a function of MOP concentration, which necessitated the use of different measurement techniques to measure the kinetics for fast (high concentration) and slow (low concentration) adsorption processes. In detail, the rapid-scan method was used for the slower MOP adsorption time constants at low concentrations, while the step-scan method was required for higher MOP concentrations due to the much shorter time constants associated with adsorption in this

regime. Here, it is important to note that the enhanced stability of the black Si-based substrates allows such step-scan measurements to be performed over multiple hours without degradation of the substrate surface.

The evolutions of the adsorption kinetics at lower MOP concentrations, recorded with the rapid-scan method, are depicted in Figure 3b. A clear trend is observed with higher MOP concentrations leading to faster adsorption on the surface of the working electrode. However, for concentrations above 333 μM , the kinetic rates approach the time limit of rapid-scan measurements and, therefore, step-scan measurements were performed. Such measurements reveal that the trend of decreasing adsorption time constants with increasing concentration continues for the higher concentrations depicted in Figure 3c. A large signal-to-noise ratio is obtained for all time-resolved measurements, confirming that the bSi-evap electrode provides sensitivities well below the monolayer limit. Thus, it is possible to directly monitor the adsorption kinetics with high sensitivity.

In addition to investigating the adsorption kinetics, we attempted to quantify the rate of MOP desorption as a function of its concentration in the bulk electrolyte. As shown in the trailing edge of the kinetic traces in Figure 3b, desorption was observed to be much faster than adsorption. Indeed, the desorption kinetics were found to be faster than the time resolution of rapid-scan measurements (60 ms). While the step-scan method would likely have sufficient time resolution for characterizing these desorption processes, the correspondingly slow adsorption kinetics render such measurements impractical. This is because the repetition rate would need to be restricted to ~ 0.05 Hz to ensure the system reaches a saturated adsorption response, while over 3000 individual steps would be needed to collect the complete interferogram. Therefore, desorption kinetics for low MOP concentrations were not quantitatively analyzed. For the case of higher MOP concentrations, such issues were not relevant since both adsorption and desorption processes occurred on similarly fast time scales (see below).

In addition to analysis of the integrated peak area with time, further insight can be gained from a detailed analysis of the evolution of the peak positions. A 2D representation of the time-resolved IR spectra recorded at a concentration of 1 mM is shown in Figure 4a. While the spectral features are identical to those shown in the steady-state spectrum, important transient changes in the line positions are observed during both adsorption and desorption. For example, as the MOP molecules adsorb on the surface, a spectral blue shift is observed for each of the three most prominent vibrational modes located at 1615, 1509, and 1308 cm^{-1} . An opposite but more pronounced red shift is also observed during desorption. The dynamics of these shifts relative to their steady-state positions are presented in Figure 4b, while selected spectra, extracted at 2 ms time intervals during adsorption and desorption, are depicted in Figure 4c,d, respectively. These results highlight the evolution of both intensity and position with time. All three modes share similar kinetics during adsorption and desorption, suggesting a common origin to the observed dynamics.

As shown in Figure 4b, the magnitude of the shift is largest for the C–O–C stretching vibrational mode near 1308 cm^{-1} , which is similar to the prior steady-state observations of the potential-dependent peak shift observed by Quirk et al.¹⁶ This shift is likely either a consequence of intermolecular

interaction, the electrochemical Stark effect, or changes in the optical properties due to partial coverage, as described by effective medium theory.⁴⁷ Distinguishing the magnitude of influence from these two factors proves to be challenging since the surface concentration of MOP is also potential-dependent.

Figure 5a summarizes all of the characteristic half-times associated with adsorption and desorption, calculated based on both the change of intensity and the position of the 1615 cm^{-1} vibrational mode for each MOP concentration. As described above, there is a clear trend toward faster time constants with

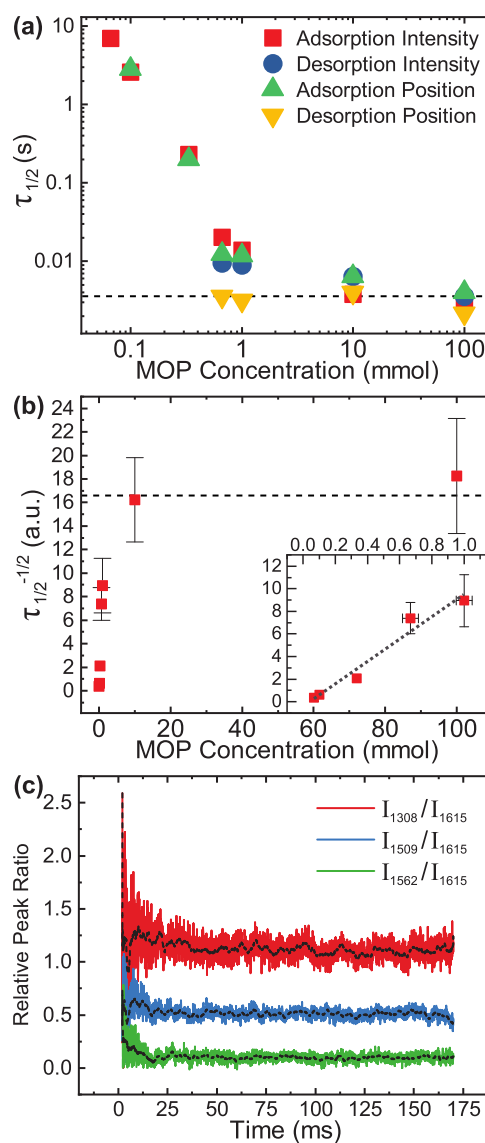


Figure 5. (a) Half-times ($\tau_{1/2}$) of the 1615 cm^{-1} peak intensities and relative peak position changes for all recorded ad- and desorption processes as a function of the MOP concentration. (b) Attempted linearization of the 1615 cm^{-1} peak intensity half-times by plotting $\tau_{1/2}^{-1/2}$ as a function of MOP concentration. The inset depicts a magnified view of the low-concentration region, which exhibits a C^{-2} relationship and therefore indicates diffusion-limited adsorption for this concentration range. The horizontal dashed lines in panels (a, b) represent the RC-limited response time of the electrochemical system. (c) Evolution of the peak intensity ratios for various vibrational modes of MOP normalized to the 1615 cm^{-1} peak for the 1 mM MOP concentration. The dotted lines in panel (c) represent linear averages to reduce the influence of noise.

increasing MOP concentrations, though this characteristic appears to saturate at high MOP concentrations. To understand this concentration-dependent behavior, we first consider the role of mass transport-limited adsorption on the observed kinetics. The Langmuir–Schaefer equation describes the time required to reach a certain surface coverage in a diffusion-limited system to be

$$t = \frac{\pi}{4D} \left(\frac{\Gamma}{C} \right)^2 \propto \frac{1}{C^2} \quad (1)$$

where D represents the diffusion constant, Γ the surface concentration of adsorbed molecules, and C the bulk concentration of the adsorbent in the surrounding liquid.^{48,49} Assuming the IR absorption peak area is linearly proportional to the concentration of adsorbed MOP molecules on the surface, the Langmuir–Schaefer equation predicts that the adsorption time constant should have a C^{-2} dependence. In the present work, we have thus attempted to linearize the concentration-dependent kinetic data by plotting $\tau_{1/2}^{-1/2}$ as a function of C , as shown in Figure 5b. While a significant deviation from the predictions of diffusion-limited adsorption is apparent for MOP concentrations >1 mM, the predicted C^{-2} dependence is observed for lower concentrations, as shown in the inset of Figure 5b.

Although several different mechanisms could lead to a deviation from the Langmuir–Schaefer dependence at higher concentrations, we find that this behavior is a consequence of the RC time constant of the system. An initial indication of this comes from the analysis of the electrical current half-time of the system without MOP, which was determined to be 3.6 ms. This is similar to the time constants observed at high MOP concentrations. To verify this, we added an external resistance in series with the working electrode and analyzed the impact on the observed MOP adsorption kinetics. As shown in Figure S7, the time constant increases linearly with added series resistance, confirming that the observed response at high MOP concentrations is not due to fundamental kinetic processes but rather due to the RC time constant of the system, consistent with prior reports on related pyridine derivatives.^{47,50} Therefore, optimizations of the electrochemical system would be required to accurately determine the adsorption and desorption mechanism kinetics in the high concentration regime, where the diffusion rate is faster than the electrical response time.

Using the diffusion constant reported for MOP in water of $1.06 \times 10^{-5} \text{ cm}^2 \text{ s}^{-1}$ along with the slope acquired through linear regression depicted in the inset of Figure 5b, one can estimate the approximate surface density of a fully established MOP monolayer, Λ .⁴¹ Carrying out this calculation and correcting for the surface roughness of the bSi-evap electrode, which yields an increase of the solid/liquid interface area of 30% relative to the geometrical area, we can estimate a molecular surface coverage of $(3.6 \pm 0.3) \times 10^{14} \text{ cm}^{-2}$ in a fully established MOP monolayer. This value corresponds to a mean molecular area of $(0.28 \pm 0.03) \text{ nm}^2$. The reported mean molecular area of similar, thiol-bound self-assembled monolayers of 4-mercaptopyridine deposited on gold is $(0.33 \pm 0.01) \text{ nm}^2$ and is, thus, comparable. The molecular orientation within these monolayers is reported to be upright with a high degree of intermolecular order, which suggests a similar structure and orientation for the presented MOP monolayers.⁵¹

Analysis of the time dependence of the relative peak areas from vibrational modes associated with on- and off-axis molecular dipoles provides further information regarding the internal structure of the MOP layer during the adsorption process. Figure 5c shows the peak area ratios of three major vibrational modes (1562, 1509, and 1308 cm^{-1}) with respect to the strongest mode at 1615 cm^{-1} for the 1 mM concentration. Running averages are depicted as dashed lines for clarity. Importantly, the observed peak ratios do not significantly change as a function of time during the potential step experiment. This observation indicates that the average orientation of MOP molecules on the working electrode surface does not change during adsorption since a change of the tilt angle would necessarily alter the orientation of the transition dipole moment with respect to the electric field of the IR radiation and thus lead to an increase or decrease of these intensity ratios. This finding indicates that intermolecular interactions do not drive the vertical molecular configuration and suggests that the σ -bonding interaction is favored over π -bonding interactions that would otherwise favor lying-down configurations.

CONCLUSIONS

Nanostructuring the Si IRE using a black Si etching method prior to electroless deposition of Au can improve the adhesion of the Au thin film, which allows for extended measurement times with similar or even moderately improved surface enhancement compared with planar systems. The roughened substrates, combined with Au layers designed for SEIRAS measurements, provide a significant improvement in sheet resistance of the active surface compared with substrates prepared by electrodeposition of Au on ITO. Therefore, black Si-based substrates can improve the response times of the electrochemical setup. This is especially relevant for the investigation of time-dependent processes, since the RC time constant presents a fundamental limit to the effective time resolution of the measurement. Here, the improved stability and conductivity enabled in-depth investigations of the adsorption kinetics of 4-methoxypyridine on the Au working electrode as a function of its concentration in the supporting electrolyte. The inverse square relationship between concentration and adsorption time constant indicates a diffusion-limited adsorption process up to a concentration of approximately 1 mM. However, the system is limited by the RC time constant at higher concentrations but is governed by the electrolyte resistance rather than that of the highly conductive black Si-based working electrode. Using this internal reflection element, we find that rapid potential step-induced adsorption does not lead to changes in molecular orientation on the working electrode during the observed time scale since the ratios of peak intensities for vibrational modes possessing transition dipole moments with different orientations with respect to the main molecular axis are approximately constant during the adsorption process. Nevertheless, changes in the peak positions are observed during both the adsorption and desorption of the MOP molecules on the surface. These transient shifts are characterized by time constants similar to those of the spectral intensity changes and are most pronounced for the vibrational transition of the methoxy group.

Overall, the presented substrate structure, comprising a black Si internal reflection element onto which electroless-deposited and evaporated layers are applied, enables highly

sensitive in situ electrochemical measurements with significantly enhanced stability, reduced sheet resistance, and improved time resolution relative to those of traditional IREs. Thus, these structures represent a powerful platform for advanced in situ electrochemical studies of solid/liquid interfaces of relevance for catalytic, energy storage, and sensing applications.

■ ASSOCIATED CONTENT

SI Supporting Information

The Supporting Information is available free of charge at <https://pubs.acs.org/doi/10.1021/acsami.3c17294>.

Schematic of the in situ electrochemical cell, additional SEM micrographs of surface morphologies at intermediate processing steps and of the finished surfaces, stability testing of working electrodes, sheet resistance of all relevant substrates under investigation, and influence of added series resistance on MOP adsorption half-time (PDF)

■ AUTHOR INFORMATION

Corresponding Authors

Felix Rauh – Walter Schottky Institute, Technical University of Munich, 85748 Garching, Germany; Physics Department, TUM School of Natural Sciences, Technical University of Munich, 85748 Garching, Germany; Email: felix.rauh@wsi.tum.de

Johannes Dittloff – Walter Schottky Institute, Technical University of Munich, 85748 Garching, Germany; Physics Department, TUM School of Natural Sciences, Technical University of Munich, 85748 Garching, Germany; orcid.org/0000-0002-8167-4546; Email: johannes.dittloff@wsi.tum.de

Ian D. Sharp – Walter Schottky Institute, Technical University of Munich, 85748 Garching, Germany; Physics Department, TUM School of Natural Sciences, Technical University of Munich, 85748 Garching, Germany; orcid.org/0000-0001-5238-7487; Email: sharp@wsi.tum.de

Authors

Moritz Thun – Walter Schottky Institute, Technical University of Munich, 85748 Garching, Germany; Physics Department, TUM School of Natural Sciences, Technical University of Munich, 85748 Garching, Germany

Martin Stutzmann – Walter Schottky Institute, Technical University of Munich, 85748 Garching, Germany; Physics Department, TUM School of Natural Sciences, Technical University of Munich, 85748 Garching, Germany

Complete contact information is available at: <https://pubs.acs.org/doi/10.1021/acsami.3c17294>

Notes

The authors declare no competing financial interest.

■ ACKNOWLEDGMENTS

F.R. and M.S. thank the Deutsche Forschungsgemeinschaft (DFG, German Research Foundation) for funding (Project Number 245845833) within the International Research Training Group IRTG 2022—Alberta Technical University of Munich School for Functional Hybrid Materials (ATUMS). I.D.S. acknowledges support from the European Research Council (ERC) under the European Union's Horizon 2020

Research and Innovation Programme (Grant Agreement No. 864234) and from the DFG under Germany's Excellence Strategy—EXC 2089/1-390776260.

■ REFERENCES

- (1) Segev, G.; Kibsgaard, J.; Hahn, C.; Xu, Z. J.; Cheng, et al. The 2022 Solar Fuels Roadmap. *J. Phys. D: Appl. Phys.* **2022**, *55*, 323003.
- (2) Sheng, H.; Oh, M. H.; Osowiecki, W. T.; Kim, W.; Alivisatos, A. P.; Frei, H. Carbon Dioxide Dimer Radical Anion as Surface Intermediate of Photoinduced CO₂ Reduction at Aqueous Cu and CdSe Nanoparticle Catalysts by Rapid-Scan FT-IR Spectroscopy. *J. Am. Chem. Soc.* **2018**, *140*, 4363–4371.
- (3) Abdellah, M.; El-Zohry, A. M.; Antila, L. J.; Windle, C. D.; Reisner, E.; Hammarström, L. Time-Resolved IR Spectroscopy Reveals a Mechanism with TiO₂ as a Reversible Electron Acceptor in a TiO₂–Re Catalyst System for CO₂ Photoreduction. *J. Am. Chem. Soc.* **2017**, *139*, 1226–1232.
- (4) Heyes, J.; Dunwell, M.; Xu, B. CO₂ Reduction on Cu at Low Overpotentials with Surface-Enhanced in situ Spectroscopy. *J. Phys. Chem. C* **2016**, *120*, 17334–17341.
- (5) Sheng, H.; Frei, H. Direct Observation by Rapid-Scan FT-IR Spectroscopy of Two-Electron-Reduced Intermediate of Tetraaza Catalyst [Co^{II}N₄H(MeCN)]²⁺ Converting CO₂ to CO. *J. Am. Chem. Soc.* **2016**, *138*, 9959–9967.
- (6) Kas, R.; Ayemoba, O.; Firet, N. J.; Middelkoop, J.; Smith, W. A.; Cuesta, A. In-situ Infrared Spectroscopy Applied to the Study of the Electrocatalytic Reduction of CO₂: Theory, Practice and Challenges. *ChemPhysChem* **2019**, *20*, 2904–2925.
- (7) Zandi, O.; Hamann, T. W. Determination of Photoelectrochemical Water Oxidation Intermediates on Haematite Electrode Surfaces Using Operando Infrared Spectroscopy. *Nat. Chem.* **2016**, *8*, 778–783.
- (8) Frei, H. Time-Resolved Vibrational and Electronic Spectroscopy for Understanding How Charges Drive Metal Oxide Catalysts for Water Oxidation. *J. Phys. Chem. Lett.* **2022**, *13*, 7953–7964.
- (9) Cuesta, A. ATR-SEIRAS for Time-Resolved Studies of Electrode–Electrolyte Interfaces. *Curr. Opin. Electrochem.* **2022**, *35*, 101041.
- (10) Sun, S.-G.; Cai, W.-B.; Wan, L.-J.; Osawa, M. Infrared Absorption Enhancement for CO Adsorbed on Au Films in Perchloric Acid Solutions and Effects of Surface Structure Studied by Cyclic Voltammetry, Scanning Tunneling Microscopy, and Surface-Enhanced IR Spectroscopy. *J. Phys. Chem. B* **1999**, *103*, 2460–2466.
- (11) Miyake, H.; Ye, S.; Osawa, M. Electroless Deposition of Gold Thin Films on Silicon for Surface-Enhanced Infrared Spectroelectrochemistry. *Electrochem. Commun.* **2002**, *4*, 973–977.
- (12) Delgado, J. M.; Orts, J. M.; Pérez, J. M.; Rodes, A. Sputtered Thin-Film Gold Electrodes for in situ ATR-SEIRAS and SERS Studies. *J. Electroanal. Chem.* **2008**, *617*, 130–140.
- (13) Andvaag, I. R.; Morhart, T. A.; Clarke, O. J. R.; Burgess, I. J. Hybrid Gold–Conductive Metal Oxide Films for Attenuated Total Reflectance Surface Enhanced Infrared Absorption Spectroscopy. *ACS Appl. Nano Mater.* **2019**, *2*, 1274–1284.
- (14) Le, F.; Brandl, D. W.; Urzhumov, Y. A.; Wang, H.; Kundu, J.; Halas, N. J.; Aizpurua, J.; Nordlander, P. Metallic Nanoparticle Arrays: A Common Substrate for both Surface-Enhanced Raman Scattering and Surface-Enhanced Infrared Absorption. *ACS Nano* **2008**, *2*, 707–718.
- (15) Rosendahl, S. M.; Danger, B. R.; Vivek, J. P.; Burgess, I. J. Surface Enhanced Infrared Absorption Spectroscopy Studies of DMAP Adsorption on Gold Surfaces. *Langmuir* **2009**, *25*, 2241–2247.
- (16) Quirk, A.; Unni, B.; Burgess, I. J. Surface Enhanced Infrared Studies of 4-Methoxypyridine Adsorption on Gold Film Electrodes. *Langmuir* **2016**, *32*, 2184–2191.
- (17) Dunwell, M.; Lu, Q.; Heyes, J. M.; Rosen, J.; Chen, J. G.; Yan, Y.; Jiao, F.; Xu, B. The Central Role of Bicarbonate in the

Electrochemical Reduction of Carbon Dioxide on Gold. *J. Am. Chem. Soc.* **2017**, *139*, 3774–3783.

(18) Huo, S.-J.; Li, Q.-X.; Yan, Chen, Y.; Cai, W.-B.; Xu, Q.-J.; Osawa, M. Tunable Surface-Enhanced Infrared Absorption on Au Nanofilms on Si Fabricated by Self-Assembly and Growth of Colloidal Particles. *J. Phys. Chem. B* **2005**, *109*, 15985–15991.

(19) Osawa, M.; Ataka, K.-i.; Yoshii, K.; Yotsuyanagi, T. Surface-Enhanced Infrared ATR Spectroscopy for in situ Studies of Electrode/Electrolyte Interfaces. *J. Electron Spectrosc. Relat. Phenom.* **1993**, *64–65*, 371–379.

(20) Osawa, M. Dynamic Processes in Electrochemical Reactions Studied by Surface-Enhanced Infrared Absorption Spectroscopy (SEIRAS). *Bull. Chem. Soc. Jpn.* **1997**, *70*, 2861–2880.

(21) Ohta, N.; Nomura, K.; Yagi, I. Electrochemical Modification of Surface Morphology of Au/Ti Bilayer Films Deposited on a Si Prism for in Situ Surface-Enhanced Infrared Absorption (SEIRA) Spectroscopy. *Langmuir* **2010**, *26*, 18097–18104.

(22) Miki, A.; Ye, S.; Osawa, M. Surface-enhanced IR Absorption on Platinum Nanoparticles: An Application to Real-time Monitoring of Electrocatalytic Reactions. *Chem. Commun.* **2002**, *2*, 1500–1501.

(23) Bjerke, A. E.; Griffiths, P. R.; Theiss, W. Surface-Enhanced Infrared Absorption of CO on Platinized Platinum. *Anal. Chem.* **1999**, *71*, 1967–1974.

(24) Delgado, J. M.; Orts, J. M.; Rodes, A. A Comparison between Chemical and Sputtering Methods for Preparing Thin-Film Silver Electrodes for in situ ATR-SEIRAS Studies. *Electrochim. Acta* **2007**, *52*, 4605–4613.

(25) Wang, H.-F.; Yan, Y.-G.; Huo, S.-J.; Cai, W.-B.; Xu, Q.-J.; Osawa, M. Seeded Growth Fabrication of Cu-on-Si Electrodes for in situ ATR-SEIRAS Applications. *Electrochim. Acta* **2007**, *52*, 5950–5957.

(26) Clarke, O. J. R.; Burgess, I. J. Electrodeposited Gold Nanodaggers on Conductive Metal Oxide Films Provide Substrates for Dual-Modality Surface Sensitive Vibrational Spectroscopy. *J. Phys. Chem. C* **2020**, *124*, 13356–13364.

(27) Geiger, S.; Kasian, O.; Mingers, A. M.; Mayrhofer, K. J. J.; Cherevko, S. Stability Limits of Tin-Based Electrocatalyst Supports. *Sci. Rep.* **2017**, *7*, No. 4595.

(28) Benck, J. D.; Pinaud, B. A.; Gorlin, Y.; Jaramillo, T. F. Substrate Selection for Fundamental Studies of Electrocatalysts and Photoelectrodes: Inert Potential Windows in Acidic, Neutral, and Basic Electrolyte. *PLoS One* **2014**, *9*, No. e107942, DOI: 10.1371/journal.pone.0107942.

(29) Ko, M.; Kim, H.-U.; Jeon, N. Boosting Electrochemical Activity of Porous Transparent Conductive Oxides Electrodes Prepared by Sequential Infiltration Synthesis. *Small* **2022**, *18*, 2105898.

(30) Clarke, O. J. R.; Rowley, A.; Fox, R. V.; Atifi, A.; Burgess, I. J. Diamonds in the Rough: Direct Surface Enhanced Infrared Spectroscopic Evidence of Nitrogen Reduction on Boron-Doped Diamond Supported Metal Catalysts. *Anal. Chem.* **2023**, *95*, 10476–10480.

(31) Morhart, T. A.; Tu, K.; Read, S. T.; Rosendahl, S. M.; Wells, G.; Achenbach, S.; Burgess, I. J. Surface Enhanced Infrared Spectroelectrochemistry Using a Microband Electrode. *Can. J. Chem.* **2022**, *100*, 495–499.

(32) Koynov, S.; Brandt, M. S.; Stutzmann, M. Black Nonreflecting Silicon Surfaces for Solar Cells. *Appl. Phys. Lett.* **2006**, *88*, 203107.

(33) Yuan, H.-C.; Yost, V. E.; Page, M. R.; Stradins, P.; Meier, D. L.; Branz, H. M. Efficient Black Silicon Solar Cell with a Density-Graded Nanoporous Surface: Optical Properties, Performance Limitations, and Design Rules. *Appl. Phys. Lett.* **2009**, *95*, 123501.

(34) Branz, H. M.; Yost, V. E.; Ward, S.; Jones, K. M.; To, B.; Stradins, P. Nanostructured Black Silicon and the Optical Reflectance of Graded-Density Surfaces. *Appl. Phys. Lett.* **2009**, *94*, 231121.

(35) Noda, H.; Ataka, K.; Wan, L.-J.; Osawa, M. Time-Resolved Surface-Enhanced Infra-red Study of Molecular Adsorption at the Electrochemical Interface. *Surf. Sci.* **1999**, *427–428*, 190–194.

(36) Berná, A.; Delgado, J. M.; Orts, J. M.; Rodes, A.; Feliu, J. M. Spectroelectrochemical Study of the Adsorption of Acetate Anions at

Gold Single Crystal and Thin-Film Electrodes. *Electrochim. Acta* **2008**, *53*, 2309–2321.

(37) Rodes, A.; Orts, J.; Pérez, J.; Feliu, J.; Aldaz, A. Sulphate Adsorption at Chemically Deposited Silver Thin Film Electrodes: Time-Dependent Behaviour as Studied by Internal Reflection Step-Scan Infrared Spectroscopy. *Electrochem. Commun.* **2003**, *5*, 56–60.

(38) Fashina, A. A.; Adama, K. K.; Oyewole, O. K.; Anye, V. C.; Asare, J.; Zebaze Kana, M. G.; Soboyejo, W. O. Surface Texture and Optical Properties of Crystalline Silicon Substrates. *J. Renewable Sustainable Energy* **2015**, *7*, 063119.

(39) Hu, Y.; Diao, X.; Wang, C.; Hao, W.; Wang, T. Effects of Heat Treatment on Properties of ITO Films Prepared by RF Magnetron Sputtering. *Vacuum* **2004**, *75*, 183–188.

(40) Morhart, T. A.; Unni, B.; Lardner, M. J.; Burgess, I. J. Electrochemical ATR-SEIRAS Using Low-Cost, Micromachined Si Wafers. *Anal. Chem.* **2017**, *89*, 11818–11824.

(41) Lange, H.; Maultzsch, J.; Meng, W.; Mollenhauer, D.; Paulus, B.; Peica, N.; Schlecht, S.; Thomsen, C. Adsorption Behavior of 4-Methoxypyridine on Gold Nanoparticles. *Langmuir* **2011**, *27*, 7258–7264.

(42) Andvaag, I. R.; Lins, E.; Burgess, I. J. An Effective Medium Theory Description of Surface-Enhanced Infrared Absorption from Metal Island Layers Grown on Conductive Metal Oxide Films. *J. Phys. Chem. C* **2021**, *125*, 22301–22311.

(43) Agrawal, A.; Singh, A.; Yazdi, S.; Singh, A.; Ong, G. K.; Bustillo, K.; Johns, R. W.; Ringe, E.; Milliron, D. J. Resonant Coupling between Molecular Vibrations and Localized Surface Plasmon Resonance of Faceted Metal Oxide Nanocrystals. *Nano Lett.* **2017**, *17*, 2611–2620.

(44) Li, Y.; Wang, D.; Liang, Z.; Zeng, L.; Li, W.; Xie, P.; Ding, Q.; Zhang, H.; Schaaf, P.; Wang, W. Evaluating the Optical Response of Heavily Decorated Black Silicon Based on a Realistic 3d Modeling Methodology. *ACS Appl. Mater. Interfaces* **2022**, *14*, 36189–36199.

(45) Gwamuri, J.; Vora, A.; Khanal, R. R.; Phillips, A. B.; Heben, M. J.; Guney, D. O.; Bergstrom, P.; Kulkarni, A.; Pearce, J. M. Limitations of Ultra-Thin Transparent Conducting Oxides for Integration Into Plasmonic-Enhanced Thin-Film Solar Photovoltaic Devices. *Mater. Renewable Sustainable Energy* **2015**, *4*, 12.

(46) *CRC Handbook of Chemistry and Physics*, 102nd ed.; Rumble, J. R., Ed.; CRC Press: Boca Raton, 2021.

(47) Lins, E.; Andvaag, I. R.; Read, S.; Rosendahl, S. M.; Burgess, I. J. Dual-Frequency Comb Spectroscopy Studies of Ionic Strength Effects in Time-Resolved ATR-SEIRAS. *J. Electroanal. Chem.* **2022**, *921*, 116672.

(48) Langmuir, I.; Schaefer, V. J. The Effect of Dissolved Salts on Insoluble Monolayers. *J. Am. Chem. Soc.* **1937**, *59*, 2400–2414.

(49) Chen, J. Simulating Stochastic Adsorption of Diluted Solute Molecules at Interfaces. *AIP Adv.* **2022**, *12*, 015318.

(50) Lins, E.; Read, S.; Unni, B.; Rosendahl, S. M.; Burgess, I. J. Microsecond Resolved Infrared Spectroelectrochemistry Using Dual Frequency Comb IR Lasers. *Anal. Chem.* **2020**, *92*, 6241–6244.

(51) Yoshimoto, S.; Ono, Y.; Kuwahara, Y.; Nishiyama, K.; Taniguchi, I. Structural Changes of 4,4'-(Dithiodibutylene)dipyridine SAM on a Au(111) Electrode with Applied Potential and Solution pH and Influence of Alkyl Chain Length of Pyridine-Terminated Thiolate SAMs on Cytochrome *c* Electrochemistry. *J. Phys. Chem. C* **2016**, *120*, 15803–15813.